Research in Astronomy and Astrophysics, 23:095006 (10pp), 2023 September https://doi.org/10.1088/1674-4527/acd7bd

Updated Inventory of Carbon Monoxide in the Taurus Molecular Cloud

Yan Duan[1,2], Di Li[1,3,4], Laurent Pagani[5], Paul F. Goldsmith[6], Tao-Chung Ching[7], Chen Wang[1], and Jinjin Xie[8]
[1] National Astronomical Observatories, Chinese Academy of Sciences, Beijing 100101, China; dili@nao.cas.cn
[2] University of Chinese Academy of Sciences, Beijing 100049, China
[3] Research Center for Intelligent Computing Platforms, Zhejiang Laboratory, Hangzhou 311100, China
[4] NAOC-UKZN Computational Astrophysics Centre, University of KwaZulu-Natal, Durban 4000, South Africa
[5] LERMA & UMR 8112 du CNRS, Observatoire de Paris, PSL University, Sorbonne Universités, CNRS, F-75014 Paris, France
[6] Jet Propulsion Laboratory, California Institute of Technology, 4800 Oak Grove Drive, Pasadena, CA 91109, USA
[7] Jansky Fellow, National Radio Astronomy Observatory, 1003 Lopezville Road, Socorro, NM 87801, USA
[8] Shanghai Astronomical Observatory, Chinese Academy of Sciences, Shanghai 200030, China
Received 2023 March 23; revised 2023 April 18; accepted 2023 April 21; published 2023 July 26

Abstract

The most extensive survey of carbon monoxide (CO) gas in the Taurus molecular cloud relied on ^{12}CO and ^{13}CO $J = 1 \rightarrow 0$ emission only, distinguishing the region where ^{12}CO is detected without ^{13}CO (named mask 1 region) from the one where both are detected (mask 2 region) (Goldsmith et al. 2008; Pineda et al. 2010). We have taken advantage of recent ^{12}CO $J = 3 \rightarrow 2$ James Clerk Maxwell Telescope observations, where they include mask 1 regions to estimate density, temperature, and N(CO) with a large velocity gradient model. This represents 1395 pixels out of ∼1.2 million in the mark 1 region. Compared to Pineda et al. (2010) results and assuming a $T_{\rm kin}$ of 30 K, we find a higher volume density of molecular hydrogen of 3.3×10^3 cm^{-3}, compared to their 250–700 cm^{-3}, and a CO column density of 5.7×10^{15} cm^{-2}, about a quarter of their value. The differences are important and show the necessity to observe several CO transitions to better describe the intermediate region between the dense cloud and the diffuse atomic medium. Future observations to extend the ^{12}CO $J = 3 \rightarrow 2$ mapping further away from the ^{13}CO-detected region comprising mask 1 are needed to revisit our understanding of the diffuse portions of dark clouds.

Key words: submillimeter: ISM – ISM: clouds – ISM: molecules

1. Introduction

Understanding star formation is one of the fundamental challenges for astrophysics. Observations indicate that stars are born in molecular clouds, relatively cold, dense regions in the interstellar medium, which exist widely throughout the Milky Way and other galaxies (e.g., Wilson et al. 1970; Dame et al. 1987, 2001; Blitz et al. 2007; Kennicutt & Evans 2012). The Taurus molecular cloud complex is a famous low-mass star-forming region about 140 pc away from us (Torres et al. 2009), which is close to us and has been widely studied with carbon monoxide (CO) and its isotopologues (e.g., Ungerechts & Thaddeus 1987; Mizuno et al. 1995; Onishi et al. 1996, 1998) and other molecules (e.g., Langer et al. 1995; Onishi et al. 2002; Tatematsu et al. 2004; Friesen et al. 2017). The proximity of Taurus allows us to accurately measure molecular gas properties, such as CO excitation and depletion, the column density and volume density of molecular hydrogen, the relationship between gas and dust, and so on. The past CO survey has provided systematic measurements of the total column density of CO, covering the largest area of the Taurus molecular cloud so far (Goldsmith et al. 2008; Pineda et al. 2010).

Goldsmith et al. (2008) published the Taurus ^{12}CO $J = 1 \rightarrow 0$ and ^{13}CO $J = 1 \rightarrow 0$ survey covering 100 deg^2 using the Five College Radio Astronomy Observatory (FCRAO) 14 m telescope. The data have become a treasure trove for the studies of turbulence (Heyer & Brunt 2012), cloud evolution (Pineda et al. 2010), filament formation (Hacar et al. 2013), and stellar feedback (Li et al. 2015). Goldsmith et al. (2008) defined different regions within the Taurus molecular cloud, which they called "mask regions," according to which isotopologues of CO were detected. Using the mask in which only ^{12}CO but no ^{13}CO emission was detected, Goldsmith et al. (2008) developed a large velocity gradient (LVG) method (Goldsmith et al. 1983) for analyzing the column density of ^{12}CO and H_2, assuming a kinetic temperature of 15 K and an optically thick ^{12}CO $J = 1 \rightarrow 0$ line. Pineda et al. (2010) combined the FCRAO CO survey data with the Two Micron All Sky Survey (2MASS) extinction data to further investigate the relationship between CO and H_2 (derived from dust extinction) in Taurus. For the mask 1 region where only ^{12}CO was detected but no ^{13}CO, they used the RADEX program in its LVG mode to calculate the column density of CO. They compared N(CO) to $N(H_2)$ to derive a varying [^{12}CO/H_2] abundance ratio.

At submillimeter wavelengths, the James Clerk Maxwell Telescope (JCMT)'s observations of mid-J CO with a high spatial dynamic range provide more possibilities for the accurate excitation and dynamic measurement of the molecular gas in Taurus. Davis et al. (2010) published CO $J=3\rightarrow2$ maps of B213–L1495 cloud and detection of 23 outflows there. Duan et al. (2023) detected a particular molecular bubble–outflow structure using JCMT ^{12}CO $J=3\rightarrow2$ observations of the Taurus B18 cloud.

In this paper, we focus on the region where ^{12}CO is detected but not ^{13}CO in individual pixels (mask 1), covering 55% of the area in Taurus where CO was detected (mask 1 and mask 2 regions). Using ^{12}CO $J=1\rightarrow0$ and $J=3\rightarrow2$ data, we can provide better CO column density measurements at the edges of Taurus B18, HCl2, and B213–L1495 clouds. We describe the observations in Section 2. We provide the measurements of N(CO) and the comparison with Pineda et al. (2010) in Section 3. We discuss the CO-derived $N(H_2)$ in Section 4. We summarize our results in Section 5.

2. Observations and Data

The data we used are displayed in Figure 1. ^{12}CO $J=3\rightarrow2$ maps are all convolved with a Gaussian kernel to obtain an angular resolution of 45″, which is the FWHM of the ^{12}CO $J=1\rightarrow0$ map. We present CO $J=1\rightarrow0$ and $J=3\rightarrow2$ observations in Sections 2.1 and 2.2, respectively.

2.1. ^{12}CO and ^{13}CO J = 1 → 0 from the FCRAO 14 m Telescope

We utilize the ^{12}CO $J=1\rightarrow0$ data observed with the 14 m FCRAO millimeter telescope, which is extracted from the 100 deg^2 FCRAO large-scale survey covering the Taurus molecular cloud (Goldsmith et al. 2008; Narayanan et al. 2008). The FWHM of the telescope beam is 45″ for the ^{12}CO $J=1\rightarrow0$ (115.271202 GHz) line and 47″ for the ^{13}CO $J=1\rightarrow0$ (110.201353 GHz). The FCRAO 14 m telescope has a circular error beam of ∼0.5° in diameter, contributing ∼25% to the signal measured from a highly extended source much larger than the main beam (Narayanan et al. 2008).

We follow the mask division of Taurus employed by Goldsmith et al. (2008) and Pineda et al. (2010). The different mask regions are divided according to whether ^{12}CO and ^{13}CO $J=1\rightarrow0$ are detected or not (Goldsmith et al. 2008, their Figure 4 and Table 1). Mask 0 represents neither ^{12}CO nor ^{13}CO detected, Mask 1 represents ^{12}CO but not ^{13}CO detected, and Mask 2 represents both ^{12}CO and ^{13}CO detected. As shown in Figure 2, mask 1 accounts for 38% of the total Taurus survey area. Here, we focus on mask 1, which includes regions in which ^{12}CO is detected but ^{13}CO is not, with T_A^* sensitivities of 0.28 and 0.125 K in velocity resolutions of 0.26 and 0.27 km s^{-1} for the ^{12}CO and ^{13}CO spectra, respectively (Goldsmith et al. 2008).

For the FCRAO 14 m telescope, the main beam efficiency η_{mb} is 45% and 48%, at 115 and 110 GHz, respectively, as determined from measurements of Jupiter (Pineda et al. 2010).

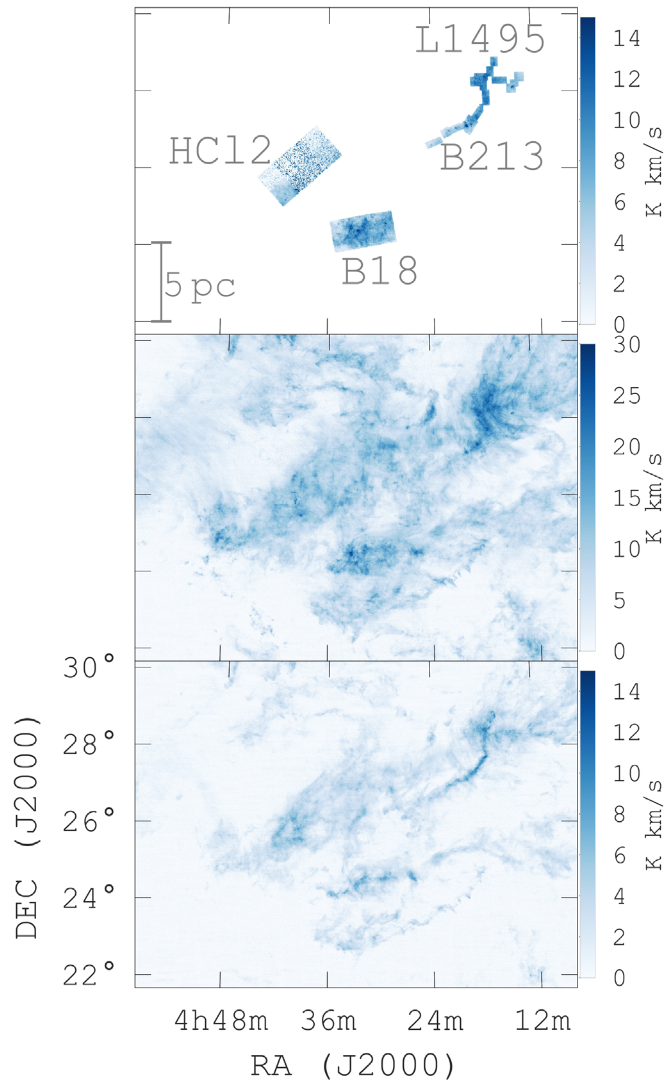

Figure 1. The ^{12}CO $J=3\rightarrow2$ (top), ^{12}CO $J=1\rightarrow0$ (middle), and ^{13}CO $J=1\rightarrow0$ (bottom) (Goldsmith et al. 2008; Narayanan et al. 2008) data employed for analysis in the Taurus molecular cloud. The ^{12}CO $J=3\rightarrow2$ map of Taurus B213–L1495 cloud has been published by Davis et al. (2010).

The forward scattering and spillover efficiency η_{fss} (Kutner & Ulich 1981) is determined by observations of the Moon, $\eta_{fss}\approx\eta_{Moon}=0.70$ (Pineda et al. 2010). Correcting for η_{fss} provides a lower limit to the true radiation temperature for reasonably spatially extended structures (Heyer et al. 1998). For observations of the Taurus molecular cloud, the source is larger than the main beam but not uniform over the Moon size of 0.5°. In most of the region, the coupling efficiency is between η_{mb} and η_{fss}. Here, we define the coupling efficiency as $\eta_{coupling}=(\eta_{mb}+\eta_{fss})/2$ and the temperature corrected for coupling efficiency $T_c = T_A^*/\eta_{coupling}$ for our CO data. Thus, we get $\eta_{coupling}=0.575$ for ^{12}CO $J=1\rightarrow0$ and $\eta_{coupling}=0.59$ for ^{13}CO $J=1\rightarrow0$.

Table 1
Basic Information on CO Observations

Emission	Source	Year	Area (deg^2)	Tau[a]	Angular Resolution (arcsecond)	η_{mb}	η_{fss}	$\eta_{coupling}$[b]	rms[c] (K)
^{12}CO $J = 3 \rightarrow 2$	B18	2017	2	0.05–0.2	14	0.61	0.77	0.69	0.63
	HCl2	2015	2.8	0.03–0.36					1.66
	B213–L1495	2007–2009	11.8	0.05–0.13					0.080.22
^{12}CO $J = 1 \rightarrow 0$	Taurus	2003–2005	100		45	0.45	0.70	0.575	0.28
^{13}CO $J = 1 \rightarrow 0$					47	0.48	0.70	0.59	0.125

Notes.
[a] The optical depth at 225 GHz, $\tau(225)$, represents the atmospheric opacity at the time of the observations. $\tau(225)$ can be converted to precipitable water vapor (PWV) using the equation $\tau(225) = 0.04\text{PWV} + 0.017$. The values of $\tau(225)$ are from CADC.
[b] We define the coupling efficiency as $\eta_{coupling} = (\eta_{mb} + \eta_{fss})/2$, where η_{fss} and η_{mb} for JCMT at 345 GHz and for FCRAO 14 m at 115 and 110 GHz are adopted from Buckle et al. (2009) and Pineda et al. (2010), respectively.
[c] rms T_A^* in K for JCMT data in B18 and HCl2 clouds were estimated at an angular resolution of 45″ and a velocity resolution of 0.26 km s^{-1}. The sensitivity of B213–L1495 ^{12}CO $J = 3 \rightarrow 2$ (at the 0.05 km s^{-1} resolution) comes from Davis et al. (2010). The sensitivities of ^{12}CO and ^{13}CO $J = 1 \rightarrow 0$ are from Goldsmith et al. (2008).

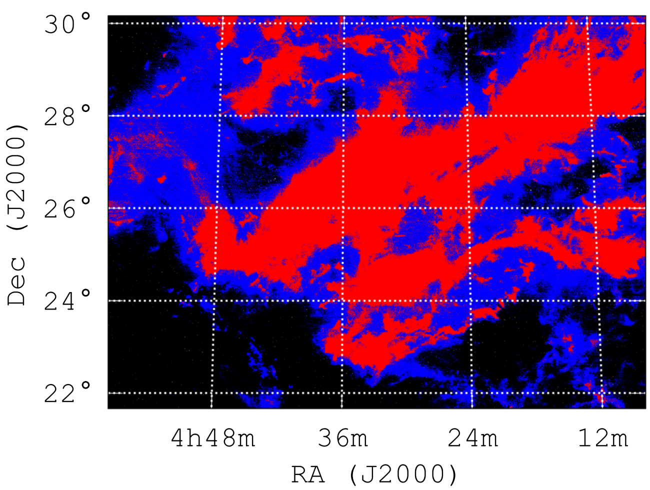

Figure 2. Mask regions in Taurus (Goldsmith et al. 2008; Pineda et al. 2010). Black represents mask 0, blue represents mask 1, and red represents mask 2.

2.2. ^{12}CO J $= 3 \rightarrow 2$ from the JCMT Telescope

We have ^{12}CO $J = 3 \rightarrow 2$ data for three regions of the Taurus molecular cloud, including B213–L1495, HCl2, and B18 from the JCMT Heterodyne Array Receiver Program (HARP) observations. The B18 cloud data are our own observations. We obtained 14 hr of JCMT HARP observation time in band 3 on 2017 September 6, 11, and 13; 2017 November 14; and 2018 August 10 (Program ID: M17BP027; M18BP072). The ^{12}CO $J = 3 \rightarrow 2$ map covers 1.4 deg^2 in the B18 cloud. Data for B213–L1495 and HCl2 are the released archive data downloaded from the Canadian Astronomy Data Centre (CADC)[9]. Davis et al. (2010) published CO $J = 3 \rightarrow 2$ data of the B213–L1495 cloud and gave a detailed analysis of the detected outflows and dense cores, as part of the JCMT legacy survey of nearby star-forming regions in the Gould Belt (Ward-Thompson et al. 2007).

The ^{12}CO $J = 3 \rightarrow 2$ transition has a rest frequency of 345.795 99 GHz. The telescope angular resolution is 14″ at this frequency, corresponding to 0.0098 pc at a distance of 140 pc. The data have been processed with the Starlink package (Currie et al. 2014). For JCMT HARP, through the observations toward the Moon in 2007, we adopt $\eta_{mb} = 61\%$ and $\eta_{fss} \approx \eta_{Moon} = 77\%$ (Buckle et al. 2009). We have $\eta_{coupling} = 0.69$ for ^{12}CO $J = 3 \rightarrow 2$. The correction for T_A^* is $1/\eta_{coupling} \approx$ 1.45. For the ^{12}CO $J = 3 \rightarrow 2$ data in these three clouds, we convolve with a Gaussian kernel to 45″, and re-grid to the angular and velocity resolutions of FCRAO ^{12}CO $J = 1 \rightarrow 0$ data. We compare the rms noise and summarize all CO observations in Table 1.

For ^{12}CO $J = 1 \rightarrow 0$ data, Goldsmith et al. (2008) have identified the CO signal and divided the map into different masks. For ^{12}CO $J = 3 \rightarrow 2$ data, we also performed signal identification for the data in three clouds, as shown in Figure 3. The main steps are as follows: (1) Draw an integrated intensity map in 0–12 km s^{-1} for each cloud. (2) Calculate the rms noise for each pixel in the map. (3) Throw away the pixels for which the signal to noise is less than 3σ for each cloud. The remaining pixels are identified as having the ^{12}CO $J = 3 \rightarrow 2$ signal. (4) Refer to the mask definition of Goldsmith et al. (2008), and select the ^{12}CO $J = 3 \rightarrow 2$ pixels in mask 1. Using the preceding steps, we select a total of 1395 pixels for the three clouds.

3. N(CO) for Mask 1

Pineda et al. (2010) divided the Taurus molecular cloud into different masks to calculate N(CO). For mask 2, where ^{12}CO

1 www.cadc-ccda.hia-iha.nrc-cnrc.gc.ca/en/search/

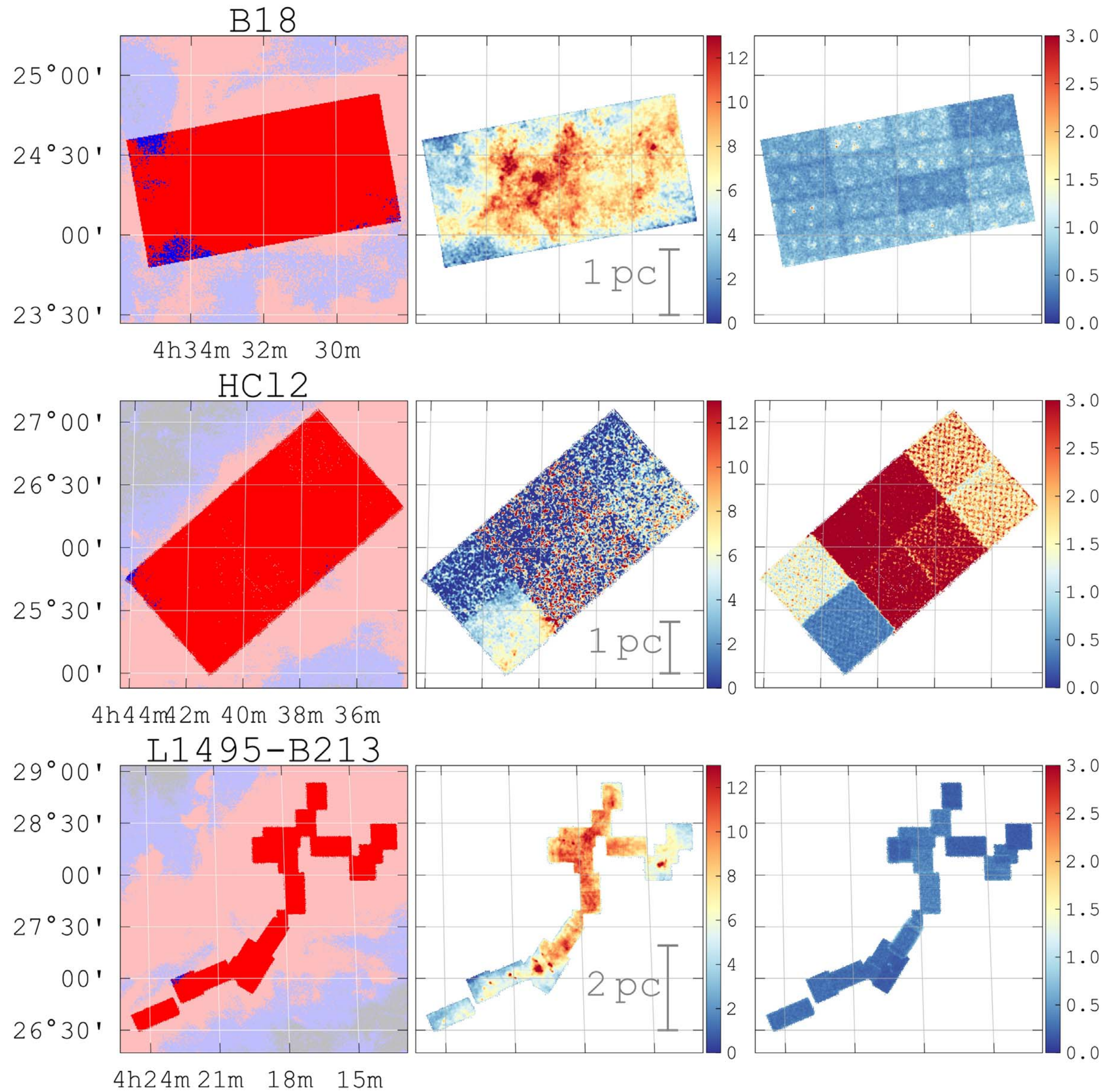

Figure 3. Images of ^{12}CO $J = 3 \rightarrow 2$ of three clouds in Taurus. The name of the cloud is labeled on the top of the first image in each row. The left column represents the mask maps. Mask 1 is defined by the blue region. The middle column represents the integrated intensity map in the velocity range from 0 to 12 km s^{-1}. The right column represents the sensitivity image of ^{12}CO $J = 3 \rightarrow 2$.

and ^{13}CO are detected in individual pixels and where density is high enough for the $J = 1 \rightarrow 0$ transitions to be thermalized, N(^{12}CO) can be determined from ^{13}CO $J = 1 \rightarrow 0$ intensities under the local thermodynamic equilibrium (LTE) assumption. For mask 1, where only ^{12}CO $J = 1 \rightarrow 0$ is detected in individual pixels, LTE does not necessarily apply. Pineda et al. (2010) binned the data into different excitation temperature ($T_{\rm ex}$) intervals and calculated N(CO) using the RADEX program under the optically thick ($\tau \gg 1$) ^{12}CO, a kinetic temperature of 15 K, and LVG assumptions.

Here, we use $J = 1 \rightarrow 0$ and $J = 3 \rightarrow 2$ transitions of ^{12}CO to independently estimate the N(CO) of mask 1, with an LVG code (originally written by Dr. Jose Cernicharo) and similar to RADEX in its LVG mode but adapted to solve the H_2 density and ^{12}CO column density from a pair of observed transitions (Castets et al. 1990). There are only 1395 pixels with both ^{12}CO $J = 1 \rightarrow 0$ and $J = 3 \rightarrow 2$ data that are located in the Taurus mask 1 region, at the edges of the B18, HCl2, and B213–L1495 clouds.

We reproduce the result of Pineda et al. (2010) in mask 1, as shown in Section 3.1. Our LVG calculation with ^{12}CO

$J = 3 \rightarrow 2$ and $J = 1 \rightarrow 0$ data is given in Section 3.2. We compare the results of the two studies in Section 3.3.

3.1. N(CO) from Pineda et al. (2010)

Instead of running the RADEX program, we only used the N(CO)$/\delta v$ and T_{ex} data in Table 1 of Pineda et al. (2010) to restore the N(CO)$/\delta v$. Here, we calculate T_{ex} using the maximum corrected antenna temperature T_c (peak) of ^{12}CO $J = 1 \rightarrow 0$ emission for every pixel according to

$$T_{ex} = \frac{5.53}{\ln\left(1 + \frac{5.53}{T_c(^{12}\mathrm{CO}) + 0.83}\right)} \quad (1)$$

(Pineda et al. 2010, their Equation (19)). With this equation, we divide the T_{ex} data of 1395 pixels into eight different T_{ex} bins. The width of each bin is 1 K. The median value in each bin ranges from 5.5 to 12.5 K. For each T_{ex} bin, all the data correspond to a value of CO column density per unit line width, $N(^{12}$CO$)/\delta v$ (see Table 1 in Pineda et al. 2010). Here, δv is the observed FWHM of the line profile (Pineda et al. 2010). We have recovered the N(CO) from $N(^{12}$CO$)/\delta v$ and δv of each pixel according to Pineda et al. (2010) and have summarized the median N(CO) in Table 2.

We define the uncertainty of N(CO) calculated by the Pineda et al. (2010) method from the rms noise of the ^{12}CO $J = 1 \rightarrow 0$ temperature. We set $T_c(^{12}$CO $J = 1 \rightarrow 0)$ + rms and $T_c(^{12}$CO $J = 1 \rightarrow 0)$ − rms as the upper and lower limits of the data value range. The differences between the two derived values of N(CO) and the original N(CO) from $T_c(^{12}$CO $J = 1 \rightarrow 0)$ are the upper and lower limits of the uncertainty.

3.2. N(CO) from the LVG Code with ^{12}CO J = 3 → 2 and J = 1 → 0

Using the LVG statistical equilibrium method (e.g., Sobolev 1960; Goldreich & Kwan 1974), our LVG code, expanded to include an inversion method (Castets et al. 1990), has been modified to adopt the collisional rate coefficients from Yang et al. (2010), the same as used by the RADEX program. These ^{12}CO collision rates include levels up to $J = 20$ and ^{12}CO collisions with both para- and ortho-H_2. When we import the line width, the kinetic temperature T_{kin}, and the temperatures of the two transitions for one molecule, this LVG code runs a grid of models. By inverting this grid, it returns $n(H_2)$ and N(CO), which are the best match for the two observed transitions.

Using this LVG code, we analyze the ^{12}CO excitation conditions through the observed T_c with two ^{12}CO lines. We assume the ^{12}CO collisions with both para- and ortho-H_2 molecules (assuming the ortho-to-para-H_2 ratio = 1), a T_{kin} of 30 K, a background temperature of 2.7 K, and helium abundance of 0.1. One of the output parameters for LVG code is the column density per unit line width, N(CO)$/\delta v$. We define the spatial variation of ^{12}CO line width δv as $\left[\int T_c(v)dv\right]/T_c(\mathrm{peak})$. There are two ^{12}CO spectral lines calculated in the code. We have two line widths, δv $(J = 1 \rightarrow 0)$ and $\delta v(J = 3 \rightarrow 2)$. We take the arithmetic mean of the two. By measuring δv in each pixel, we calculate the N(CO) for all data pixel by pixel. For the B18, HCl2, and B213–L1495 regions in Taurus, there are a total of 1395 pixels in mask 1 for calculation. For the B213–L1495 cloud, ^{12}CO $J = 3 \rightarrow 2$ emissions within the mask 1 region are limited to the B213 cloud. The median N(CO) for each cloud and the median N(CO) in these three clouds are summarized in Table 2.

The kinetic temperature T_{kin} cannot be measured directly at the edge of the cloud because of a lack of data, such as NH_3 and HC_3N hyperfine components (e.g., Li & Goldsmith 2012; Wang et al. 2020; Xie et al. 2021). The LVG code requires us to assume a T_{kin}. We find that the assumed T_{kin} is anticorrelated with the derived $n(H_2)$. This trend has also been demonstrated in the past analysis of multilevel lines of CO with RADEX (Goldsmith 2013). We compare the results under different T_{kin} assumptions, as shown in Figure 4. The results indicate that when T_{kin}= 15 K, our LVG code calculates a large $n(H_2)$ above 1×10^4 cm^{-3} because of the CO $J = 3 \rightarrow 2$ data. When we assume $T_{kin} \geqslant 30$ K, $n(H_2)$ drops below 3.3×10^3 cm^{-3} and is relatively close to each other, yielding more reasonable but still high densities. This may be an indication that the single density model adopted is not adequate. And more sophisticated modeling, including density inhomogeneities on a scale not resolved by telescope beams, is required but beyond the scope of the present study. N(CO)$/\delta v$ is about 4.1×10^{15} to 3.3×10^{15} cm^{-2} from 15 to 50 K, the difference of which is small. Here, we assume T_{kin} to be 30 K, the derived median $n(H_2)$ is 3.3×10^3 cm^{-3}, and median N(CO)$/\delta v$ is 3.4×10^{15} cm^{-2}. When T_{kin} is assumed to be 15 K as Pineda et al. (2010), $n(H_2)$ would increase by 327%, and N(CO)$/\delta v$ would increase by 119%. In dark cloud B5, Young et al. (1982) found that T_{kin} rises from 15 K in the cloud center to 40 K at the cloud edge, with $n(H_2)$ close to 2000 cm^{-3} at the cloud edge, essentially the same as in the bulk of the cloud. Therefore, we consider that our assumption of 30 K for T_{kin} in mask 1 is reasonable.

We bin $n(H_2)$ and N(CO)$/\delta v$ from the LVG code into different T_c (^{12}CO $J = 1 \rightarrow 0$) bins to show their trend with T_c, as shown in Figure 5. For each T_c bin, the median $n(H_2)$ and N(CO)$/\delta v$ are given and shown as black solid lines. It is reasonable that N(CO)$/\delta v$ increases steadily with the increase of T_c (^{12}CO $J = 1 \rightarrow 0$), and the same trend is found in Figure 3 of Pineda et al. (2010). The value of $n(H_2)$ does not change significantly with the increase of T_c. It is largely determined by the observed ratio of the two ^{12}CO transitions, which is almost constant. The magenta dotted lines in Figure 5 represent the result under the assumption of 100% para-H_2. Compared to collisions with 50% para- and 50% ortho-H_2 molecules (ortho-to-para-H_2 ratio = 1), when 100% para-H_2 is assumed (ortho-to-para-H_2 ratio = 0), $n(H_2)$

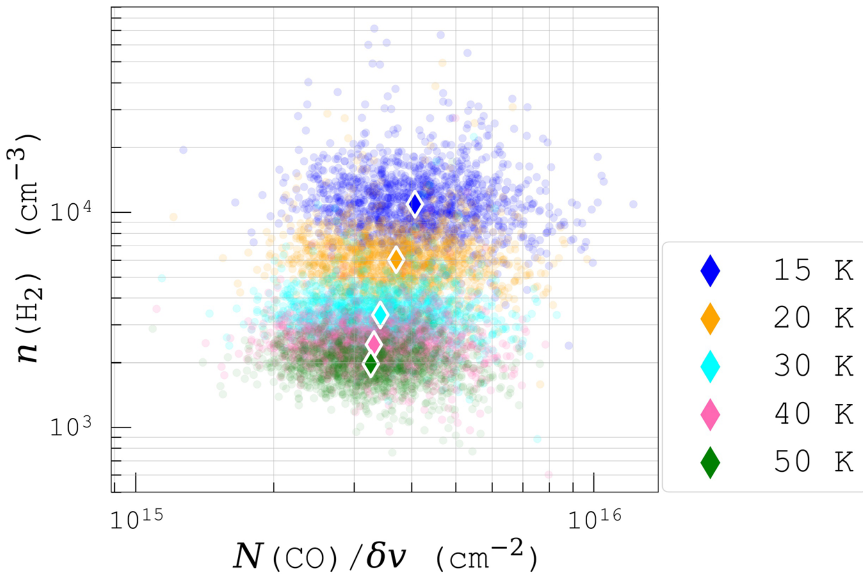

Figure 4. $n(\mathrm{H_2})$ and $N(\mathrm{CO})/\delta v$ for all data calculated under different T_{kin} assumptions. Diamond of the same color represents the median of all data for each T_{kin}.

Table 2
Physical Parameters in Mask 1 with the CO $J = 3 \rightarrow 2$ and $J = 1 \rightarrow 0$ Regions

Region	Pixel Number	Paper for N(CO)	$n(\mathrm{H_2})$ (1×10^3 cm^{-3})	N(CO) (1×10^{15} cm^{-2})	$N(\mathrm{H_2})$ (1×10^{20} cm^{-2})
B18	1276	Our	$3.3^{+8.9}_{-2.2}$	$5.8^{+2.1}_{-1.2}$	$7.2^{+0.2}_{-0.1}$
		Pineda et al.		$24.6^{+14.9}_{-11.7}$ (24%)	$8.6^{+0.9}_{-0.8}$ (84%)
HCl2	25	Our	$7.8^{+34.9}_{-4.2}$	$6.0^{+2.0}_{-1.2}$	$7.2^{+0.2}_{-0.1}$
		Pineda et al.		$23.4^{+21.4}_{-3.6}$ (26%)	$8.5^{+1.3}_{-0.2}$ (85%)
B213–L1495	94	Our	$3.2^{+4.2}_{-1.3}$	$3.2^{+1.1}_{-0.8}$	$7.0^{+0.1}_{-0.07}$
		Pineda et al.		$11.9^{+7.3}_{-4.7}$ (27%)	$7.7^{+0.5}_{-0.4}$ (91%)
Above three clouds	1395	Our	$3.3^{+7.0}_{-1.8}$	$5.7^{+1.8}_{-0.4}$	$7.2^{+0.1}_{-0.04}$
		Pineda et al.		$23.5^{+5.8}_{-15.3}$ (24%)	$8.5^{+0.4}_{-1.1}$ (85%)

Note. We defined the correction of our result to the result of Pineda et al. (2010) as the percentage given in parentheses.

becomes 114% of its original value, and $N(\mathrm{CO})/\delta v$ is practically constant.

We calculated the thermal pressure ($\langle P_{\mathrm{th}}/k \rangle = nT$) to be about 10^5 K cm^{-3}, which is almost the highest in the observed thermal pressure deduced from ^{12}CO and ^{13}CO observations of molecular clouds in the Galactic plane, $\sim 10^4$–10^5 K cm^{-3} (Sanders et al. 1993; Wolfire et al. 2010). This is possibly because the cloud here may be out of thermal equilibrium, so the pressure reflects approximate but incomplete thermal pressure balance. In Figure 6, the nonthermal line width of the average ^{13}CO $J = 1 \rightarrow 0$ spectrum also demonstrates that the Taurus mask 1 region may deviate from the thermal pressure balance.

In our calculation, we mainly consider the uncertainties of N(CO) and $n(\mathrm{H_2})$ from three aspects, which have proportional or inverse effects on N(CO) and $n(\mathrm{H_2})$. Taking these three factors together into account, we define the value range for each data to estimate uncertainties. The specific explanations are as follows:

1. The most significant uncertainty comes from the rms noise of the temperature. As in the discussion in Section 3.1, our LVG code requires input ^{12}CO $J = 1 \rightarrow 0$ and ^{12}CO $J = 3 \rightarrow 2$ temperatures. If we consider $T_{\mathrm{c}}(J = 1 \rightarrow 0)$ − rms and $T_{\mathrm{c}}(J = 3 \rightarrow 2)$ + rms, the code outputs the smaller N(CO) and the larger $n(\mathrm{H_2})$, compared to the result of $T_{\mathrm{c}}(J = 1 \rightarrow 0)$ and $T_{\mathrm{c}}(J = 3 \rightarrow 2)$. When we consider instead $T_{\mathrm{c}}(J = 1 \rightarrow 0)$ + rms and $T_{\mathrm{c}}(J = 3 \rightarrow 2)$ − rms, the code provides larger N(CO) and smaller $n(\mathrm{H_2})$. We define the computed N(CO) and $n(\mathrm{H_2})$ in this way as the upper and lower limits for the range of data values, respectively.
2. The calculation of N(CO) requires the line width δv. We take the arithmetic mean of $\delta v(J = 1 \rightarrow 0)$ and δv

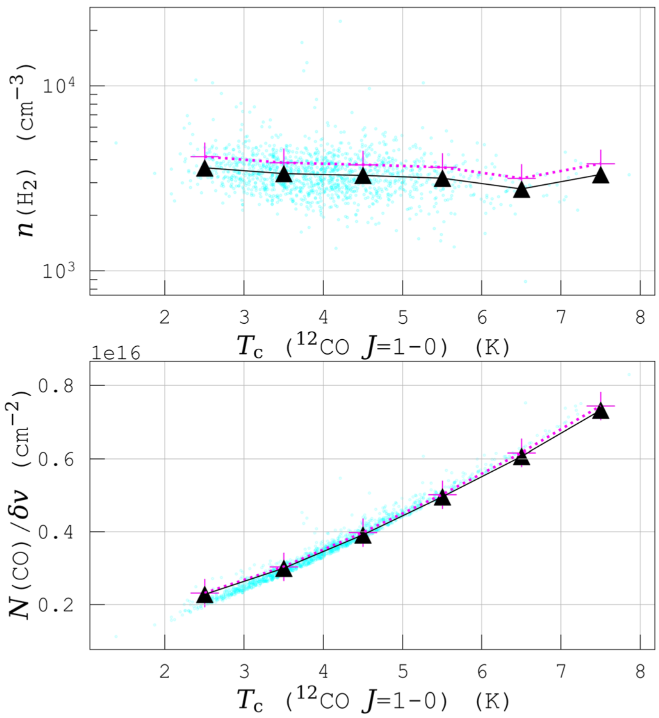

Figure 5. $n(H_2)$ (top) and $N(CO)/\delta v$ (bottom) of mask 1 binned by T_c (^{12}CO $J = 1 \rightarrow 0$) (in 1 K bins). The cyan points are the T_c, $n(H_2)$, and $N(CO)/\delta v$ determined for the 1395 pixels in mask 1. Black triangles and solid lines are the median of each T_c bin under the assumption of ortho-to-para-H_2 ratio = 1. Magenta crosses and dotted lines are the median values under the assumption of ortho-to-para-H_2 ratio = 0.

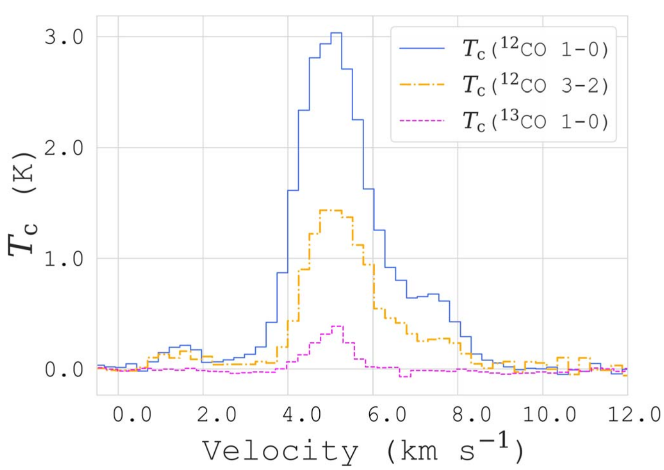

Figure 6. Average ^{12}CO, ^{13}CO $J = 1 \rightarrow 0$, and ^{12}CO $J = 3 \rightarrow 2$ spectral lines for Taurus B18 cloud within the mask 1 region, containing a total of 1276 pixels.

($J = 3 \rightarrow 2$) in our calculation. Here, we put the larger δv of both $T_c(J = 1 \rightarrow 0)$ and $T_c(J = 3 \rightarrow 2)$ in the calculation to get the upper limit of the N(CO) range. We take the smaller one of the two individual δv to calculate the lower limit of the N(CO) range.

3. The T_{kin} assumption is also relevant to the calculation results. According to Figure 4, $T_{kin} = 15$ K would lead to a large $n(H_2)$. Therefore, we choose 30 ± 10 K as a reasonable T_{kin} range.

We have run the LVG code with these $T_c \pm$ rms noise, δv, and T_{kin} simultaneously, and we obtain a range of data for N(CO) and $n(H_2)$. For each group of data, we define the median value as the result. The upper and lower limits of the range for this median pixel are found. The upper and lower uncertainties for each dataset are the differences between the upper and lower limits of the range and the median value, respectively. The median values of $n(H_2)$ and N(CO) and their uncertainties are summarized in Table 2.

3.3. Comparison of N(CO) Under the Two Methods

The free parameters in Pineda et al. (2010) are $n(H_2)$, $N(^{12}CO)/\delta v$, and the ^{12}CO/^{13}CO abundance ratio. The observable parameters are ^{12}CO $J = 1 \rightarrow 0$ and ^{13}CO $J = 1 \rightarrow 0$ intensities. The free parameters in our study are $n(H_2)$ and $N(^{12}CO)/\delta v$. The observable parameters are ^{12}CO $J = 1 \rightarrow 0$ and ^{12}CO $J = 3 \rightarrow 2$ temperatures. Observations of the $J = 1 \rightarrow 0$ and $J = 3 \rightarrow 2$ lines can output a single group of the best-fitted $n(H_2)$ and $N(^{12}CO)/\delta v$ within the inverted grid of models.

We compare the histograms of N(CO) for the three clouds B18, B213–L1495, and HCl2 and the general results in Figure 7. In Table 2, we summarize the N(CO) and $n(H_2)$ from our data, the N(CO) from Pineda et al. (2010), and the correction ratio between the two sets. We compare the following aspects for the results of these two studies in what follows:

1. Overall, N(CO) calculated presently is $5.7^{+1.8}_{-0.4} \times 10^{15}$ cm^{-2}, which is 0.24 times of the results from Pineda et al. (2010), $2.35^{+0.58}_{-1.53} \times 10^{16}$ cm^{-2}. In the diffuse portion of the molecular clouds, the N(CO) for mask 1 from either work is comparable.
2. The two studies assume different values of T_{kin}. The assumption of Pineda et al. (2010), $T_k = 15$ K, is not satisfactory here, as it would result in $n(H_2)$ of 10^4 cm^{-3}, which is far too high for regions at the edge of clouds, which are considered to be not dense. Our result of $n(H_2)=3.3^{+7.0}_{-1.8} \times 10^3$ cm^{-3} at $T_{kin}= 30$ K is somewhat higher than that of Pineda et al. (2010), but it is not unreasonable. A similar finding at the edge of the dark cloud B5 has been published by Young et al. (1982).
3. The measurement of the thermal pressure ($\langle P_{th}/k\rangle = nT$) of the gas from Pineda et al. (2010) is between 4×10^3 and 1×10^4 K cm^{-3} (with an $n(H_2)$ range of 250–700 cm^{-3}). Our value of $\langle P_{th}/k\rangle = 10^5$ K cm^{-3} is still within a reasonable range of the observed thermal

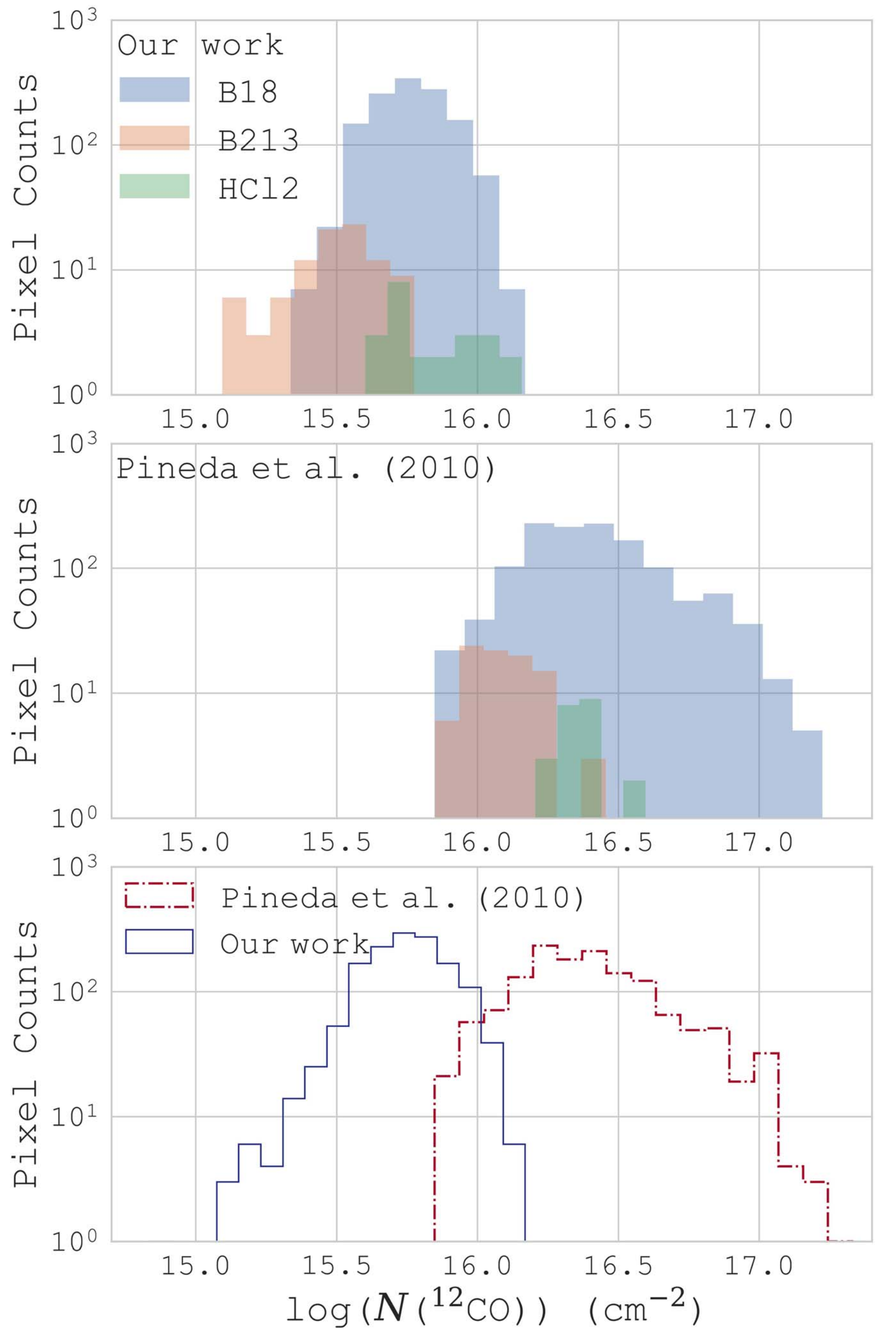

Figure 7. Histograms of ^{12}CO column density N(CO) from our calculation by the LVG code (top) and the result from Pineda et al. (2010) by the RADEX program (middle) for the B18 (blue), B213–L1495 (orange), and HCl2 (green) clouds within the Taurus mask 1 region. Comparison of our result (blue solid line) and Pineda et al. (2010) (red dashed–dotted line) methods of the three clouds with a total of 1395 pixels (bottom).

pressure for molecular clouds in the Galactic plane (Sanders et al. 1993).

Among the three clouds in Taurus, B18 includes a large amount of data, with a good sensitivity. Both of the calculation methods indicate that the N(CO) in the B213 cloud is lower than in the other two regions. The limited number of selected pixels may be located where the gas is more diffuse. It does not represent the case of the entire B213 cloud.

4. Discussion

For low column density regions, such as mask 1 and mask 0, fractional abundance of carbon monoxide, $[CO/H_2]$, may vary

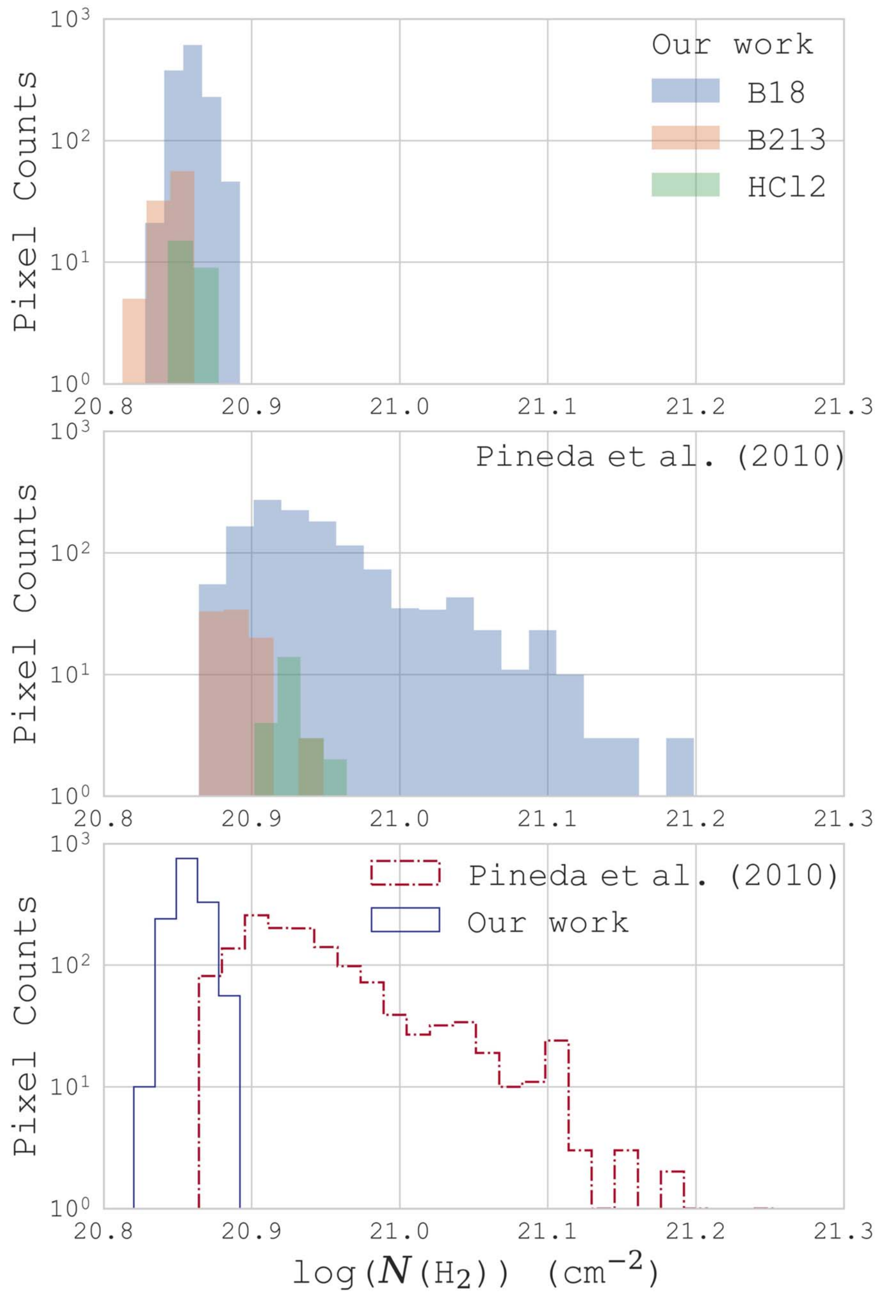

Figure 8. Histograms of $N(H_2)$ from our calculation with the LVG code (top panel) and the result of Pineda et al. (2010) by the RADEX program (middle panel) for the B18 (blue), B213–L1495 (orange), and HCl2 (green) clouds within the Taurus mask 1 region. Comparison of the $N(H_2)$ from our (blue solid line) and Pineda et al. (2010) (red dashed–dotted line) results for the three clouds with a total of 1395 pixels (bottom panel).

with CO column density over a wide range. For mask 1, Pineda et al. (2010) used 2MASS extinction to convert to $N(H_2)$, assuming $N(H_2)/A_V = 9.4 \times 10^{20}\,\mathrm{cm^{-2}\,mag^{-1}}$ (Bohlin et al. 1978), and fitted a relation between $N(H_2)$ and $N(CO)$. We apply the same $N(CO)$–$N(H_2)$ relation from Pineda et al. (2010). For every pixel, we have derived $N(H_2)$ corresponding to all $N(CO)$ data according to the equation, $\log(N(H_2)) = 0.038\,87 \times \log(N(CO))^3 - 1.779 \times \log(N(CO))^2 + 27.175 \times \log(N(CO)) - 117.71$, from Figure 14 of Pineda et al. (2010). Uncertainties of $N(H_2)$ come from the $N(CO)$ range of values. We input the upper and lower limits of the $N(CO)$ range into this equation to calculate the upper and lower limits of the $N(H_2)$ range. We summarize the median $N(H_2)$ data and their uncertainties for both studies in Figure 8 and Table 2.

In our calculation, the median CO-derived $N(H_2)$ is $7.2^{+0.1}_{-0.04} \times 10^{20}\,\mathrm{cm^{-2}}$, which is 85% of the Pineda et al. (2010)

results. The $N(H_2)$ results are not much different between the two studies, even though our N(CO) is 24% of Pineda et al. (2010) N(CO). These N(CO) data cannot accurately measure the changes in $N(H_2)$. This is because the $N(H_2)$–N(CO) conversion is insensitive in the range of $\sim 10^{15}$ to 10^{16} cm^{-2}. When N(CO) decreases 10 times, $N(H_2)$ decreases only 0.9 times. Here, we conclude that there is almost no change in CO-derived $N(H_2)$ compared to Pineda et al. (2010).

However, there is a large difference in the H_2 density and kinetic temperature between the two studies. While Pineda et al. (2010) found densities around 500 cm^{-3} for a temperature of 15 K, we found densities six times higher and a temperature approximately two times higher. The $J = 3 \rightarrow 2$ ^{12}CO observations bring important constraints, which questions the previous study. However, our observations are close to the edges of the clouds and may not be representative of the mask 1 region (no ^{13}CO detected) in general.

5. Conclusions

In the Taurus molecular cloud, we estimated the N(CO), $n(H_2)$, and $N(H_2)$ in the non-^{13}CO detection region using JCMT ^{12}CO $J = 3 \rightarrow 2$ and FCRAO ^{12}CO $J = 1 \rightarrow 0$ survey data (Goldsmith et al. 2008; Narayanan et al. 2008; Davis et al. 2010). Our measurements include parts of the edges of the B18, HCl2, and B213–L1495 clouds, containing a total of 1395 pixels. We draw the following conclusions:

1. In mask 1, we have run an LVG code with ^{12}CO $J = 1 \rightarrow 0$ and $J = 3 \rightarrow 2$ data to calculate an N(CO) of $5.7^{+1.8}_{-0.4} \times 10^{15}$ cm^{-2}, about 24% of Pineda et al. (2010) finding. We estimated $n(H_2)$ to be $3.3^{+7.0}_{-1.8} \times 10^3$ cm^{-3} under the assumption of $T_{\rm kin} = 30$ K.
2. We have estimated the $N(H_2)$ pixel by pixel, using the N(CO)–$N(H_2)$ relation (Pineda et al. 2010). The derived $N(H_2)$ almost did not change from the result of Pineda et al. (2010). The median $N(H_2)$ is $7.2^{+0.1}_{-0.04} \times 10^{20}$ cm^{-2}.

Overall, the calculation of N(CO) and $n(H_2)$ and the assumption of $T_{\rm kin}$ in mask 1 in Pineda et al. (2010) are different from ours. Using two transitions of ^{12}CO data, we measured a lower N(CO) and a higher $n(H_2)$, assuming a higher $T_{\rm kin}$. This measurement of only 1395 pixels is suggestive for future studies of the physical conditions of cloud edges for dark clouds, like Taurus. More sky area coverage and more systematic measurements are needed.

Acknowledgments

This work was supported by the National Natural Science Foundation of China (NSFC, grant Nos. 11988101, 11725313, and U1931117) and the International Partnership Program of Chinese Academy of Sciences (grant No. 114A11KYSB20210010). This research was carried out in part at the Jet Propulsion Laboratory, which is operated by the California Institute of Technology under a contract with the National Aeronautics and Space Administration (80NM0018D0004). C.W. is supported by the Natural Science Foundation of Jiangsu Province (grant No. BK20201108).

ORCID iDs

Yan Duan https://orcid.org/0000-0003-3758-7426
Laurent Pagani https://orcid.org/0000-0002-3319-1021
Jinjin Xie https://orcid.org/0000-0002-2738-146X

References

Blitz, L., Fukui, Y., Kawamura, A., et al. 2007, in Protostars and Planets V, ed. B. Reipurth, D. Jewitt, & K. Keil (Tucson: Univ. Arizona Press), 81
Bohlin, R. C., Savage, B. D., & Drake, J. F. 1978, ApJ, 224, 132
Buckle, J. V., Hills, R. E., Smith, H., et al. 2009, MNRAS, 399, 1026
Castets, A., Duvert, G., Dutrey, A., et al. 1990, A&A, 234, 469
Currie, M. J., Berry, D. S., Jenness, T., et al. 2014, in ASP Conf. Ser. 485, Astronomical Data Analysis Software and Systems XXIII, ed. N. Manset & P. Forshay (San Francisco, CA: ASP), 391
Dame, T. M., Hartmann, D., & Thaddeus, P. 2001, ApJ, 547, 792
Dame, T. M., Ungerechts, H., Cohen, R. S., et al. 1987, ApJ, 322, 706
Davis, C. J., Chrysostomou, A., Hatchell, J., et al. 2010, MNRAS, 405, 759
Duan, Y., Li, D., Goldsmith, P. F., et al. 2023, ApJ, 943, 182
Friesen, R. K., Pineda, J. E., co-PIs, et al. 2017, ApJ, 843, 63
Goldreich, P., & Kwan, J. 1974, ApJ, 189, 441
Goldsmith, P. F. 2013, ApJ, 774, 134
Goldsmith, P. F., Heyer, M., Narayanan, G., et al. 2008, ApJ, 680, 428
Goldsmith, P. F., Young, J. S., & Langer, W. D. 1983, ApJS, 51, 203
Hacar, A., Tafalla, M., Kauffmann, J., & Kovács, A. 2013, A&A, 554, A55
Heyer, M. H., Brunt, C., Snell, R. L., et al. 1998, ApJS, 115, 241
Heyer, M. H., & Brunt, C. M. 2012, MNRAS, 420, 1562
Kennicutt, R. C., & Evans, N. J. 2012, ARA&A, 50, 531
Kutner, M. L., & Ulich, B. L. 1981, ApJ, 250, 341
Langer, W. D., Velusamy, T., Kuiper, T. B. H., et al. 1995, ApJ, 453, 293
Li, D., & Goldsmith, P. F. 2012, ApJ, 756, 12
Li, H., Li, D., Qian, L., et al. 2015, ApJS, 219, 20
Mizuno, A., Onishi, T., Yonekura, Y., et al. 1995, ApJL, 445, L161
Narayanan, G., Heyer, M. H., Brunt, C., et al. 2008, ApJS, 177, 341
Onishi, T., Mizuno, A., Kawamura, A., Ogawa, H., & Fukui, Y. 1996, ApJ, 465, 815
Onishi, T., Mizuno, A., Kawamura, A., Ogawa, H., & Fukui, Y. 1998, ApJ, 502, 296
Onishi, T., Mizuno, A., Kawamura, A., Tachihara, K., & Fukui, Y. 2002, ApJ, 575, 950
Pineda, J. L., Goldsmith, P. F., Chapman, N., et al. 2010, ApJ, 721, 686
Sanders, D. B., Scoville, N. Z., Tilanus, R. P. J., Wang, Z., & Zhou, S. 1993, in AIP Conf. Ser. 278, Back to the Galaxy, ed. S. S. Holt & F. Verter (Melville: AIP), 311
Sobolev, V. V. 1960, Moving Envelopes of Stars (Cambridge, MA: Harvard Univ. Press)
Tatematsu, K., Umemoto, T., Kandori, R., & Sekimoto, Y. 2004, ApJ, 606, 333
Torres, R. M., Loinard, L., Mioduszewski, A. J., & Rodríguez, L. F. 2009, ApJ, 698, 242
Ungerechts, H., & Thaddeus, P. 1987, ApJS, 63, 645
Wang, S., Ren, Z., Li, D., et al. 2020, MNRAS, 499, 4432
Ward-Thompson, D., Di Francesco, J., Hatchell, J., et al. 2007, PASP, 119, 855
Wilson, R. W., Jefferts, K. B., & Penzias, A. A. 1970, ApJL, 161, L43
Wolfire, M. G., Hollenbach, D., & McKee, C. F. 2010, ApJ, 716, 1191
Xie, J., Fuller, G. A., Li, D., et al. 2021, SCPMA, 64, 279511
Yang, B., Stancil, P. C., Balakrishnan, N., & Forrey, R. C. 2010, ApJ, 718, 1062
Young, J. S., Goldsmith, P. F., Langer, W. D., Wilson, R. W., & Carlson, E. R. 1982, ApJ, 261, 513